DNA-mediated engineering of multicomponent enzyme crystals

Jeffrey D. Brodin[a,b], Evelyn Auyeung[b,c], and Chad A. Mirkin[a,b,c,1]

Departments of [a]Chemistry and [c]Materials Science and Engineering, and [b]International Institute for Nanotechnology, Northwestern University, Evanston, IL 60208

Contributed by Chad A. Mirkin, February 20, 2015 (sent for review January 19, 2015; reviewed by Matthew B. Francis and Chengde Mao)

The ability to predictably control the coassembly of multiple nanoscale building blocks, especially those with disparate chemical and physical properties such as biomolecules and inorganic nanoparticles, has far-reaching implications in catalysis, sensing, and photonics, but a generalizable strategy for engineering specific contacts between these particles is an outstanding challenge. This is especially true in the case of proteins, where the types of possible interparticle interactions are numerous, diverse, and complex. Herein, we explore the concept of trading protein–protein interactions for DNA–DNA interactions to direct the assembly of two nucleic-acid–functionalized proteins with distinct surface chemistries into six unique lattices composed of catalytically active proteins, or of a combination of proteins and DNA-modified gold nanoparticles. The programmable nature of DNA–DNA interactions used in this strategy allows us to control the lattice symmetries and unit cell constants, as well as the compositions and habit, of the resulting crystals. This study provides a potentially generalizable strategy for constructing a unique class of materials that take advantage of the diverse morphologies, surface chemistries, and functionalities of proteins for assembling functional crystalline materials.

nanoscience | biomaterials | self-assembly | superlattice | DNA-programmable assembly

DNA-mediated assembly strategies (1–3) that take advantage of rigid building blocks, functionalized with oriented oligonucleotides to create entities with well-defined "valencies," have emerged as powerful new ways for programming the formation of crystalline materials (4, 5). With such methods, one can make architectures with well-defined lattice parameters (6–12), symmetries (4, 8, 10, 12), and compositions (10, 12, 13), but to date they have been confined primarily to the use of hard inorganic nanoparticles (NPs) or highly branched pure nucleic-acid materials (2, 14, 15). In contrast, Nature's most powerful and versatile nanostructured building blocks are proteins and are used to effect the vast majority of processes in living systems (16). Unlike most inorganic NP systems, proteins can be made in pure and perfectly monodisperse form, making them ideal synthons for supramolecular assemblies. However, the ability to engineer lattices composed of multiple proteins, or of proteins and inorganic nanomaterials, has been limited, and the choice of protein building blocks is often restricted by structural constraints, which limits the catalytic functionalities that can be incorporated into these structures. Currently, the primary methods for making protein lattices have relied on the use of natural protein–protein interactions (17), interactions between proteins and ligands on the surfaces of inorganic NPs (17, 18), metal coordination chemistry (19), small molecule ligand–protein interactions (20–23), genetically fusing protein complexes with specific symmetries (24, 25), or DNA-mediated assembly of viruses (26, 27). Here, we introduce a new method for effecting protein crystallization by trading protein–protein interactions for complementary oligonucleotide–oligonucleotide interactions. By using different proteins functionalized with the appropriate oligonucleotides, along with the design rules introduced for inorganic systems (7, 8, 28), we show that different combinations of DNA-functionalized enzymes, and enzymes and inorganic NPs, can be assembled deliberately into preconceived lattices and, in some cases, well-defined crystal habits. Importantly, the enzymes retain their native structures and catalytic functionalities after extensive modification of their surfaces with DNA and assembly into crystalline superlattices. This work is a convincing demonstration for how DNA can be used for assembling many readily accessible functional proteins into ordered materials, regardless of their atomic compositions.

DNA-mediated NP assembly and crystallization, as developed by us (1, 4) and others (5), requires that the surface of the component building blocks be modified with a dense monolayer of radially oriented oligonucleotides. This architecture, also referred to as a programmable atom equivalent (28) or a spherical nucleic acid (SNA)–NP conjugate, enables the formation of multivalent interactions between particles hybridized to linker strands bearing short complementary sticky ends (Fig. 1 and Fig. S1). When NPs bearing complementary sticky ends are combined, heated to a temperature sufficient to disrupt these multivalent interactions, and then slowly cooled to room temperature, the reversible formation of many individually weak interparticle interactions collectively favor the formation of thermodynamically stable single-crystalline superlattices over kinetically trapped amorphous aggregates (11). Based on this principle, the inclusion of functional proteins into DNA-mediated superlattices should be possible, provided that their surfaces can be sufficiently functionalized with oligonucleotides while leaving their native structures intact, which is crucial to maintaining their functionality. To test this hypothesis, we implemented a two-step reaction scheme for appending oligonucleotides to protein surfaces under

Significance

Due to their unique structures and diverse catalytic functionalities, proteins represent a nearly limitless set of precursors for constructing functional supramolecular materials. However, programming the assembly of even a single protein into ordered superlattices is a difficult task, and a generalizable strategy for coassembling multiple proteins with distinct surface chemistries, or proteins and inorganic nanoparticles, does not currently exist. Here, we use the high-fidelity interactions characteristic of DNA–DNA "bonds" to direct the assembly of two proteins into six unique superlattices composed of either a single protein, multiple proteins, or proteins and gold nanoparticles. Significantly, the DNA-functionalized proteins retain their native catalytic functionalities both in the solution and crystalline states.

Author contributions: J.D.B., E.A., and C.A.M. designed research; J.D.B. and E.A. performed research; J.D.B., E.A., and C.A.M. analyzed data; and J.D.B. and C.A.M. wrote the paper.

Reviewers: M.B.F., University of California, Berkeley; and C.M., Purdue University.

The authors declare no conflict of interest.

[1]To whom correspondence should be addressed. Email: chadnano@northwestern.edu.

This article contains supporting information online at www.pnas.org/lookup/suppl/doi:10.1073/pnas.1503533112/-/DCSupplemental.

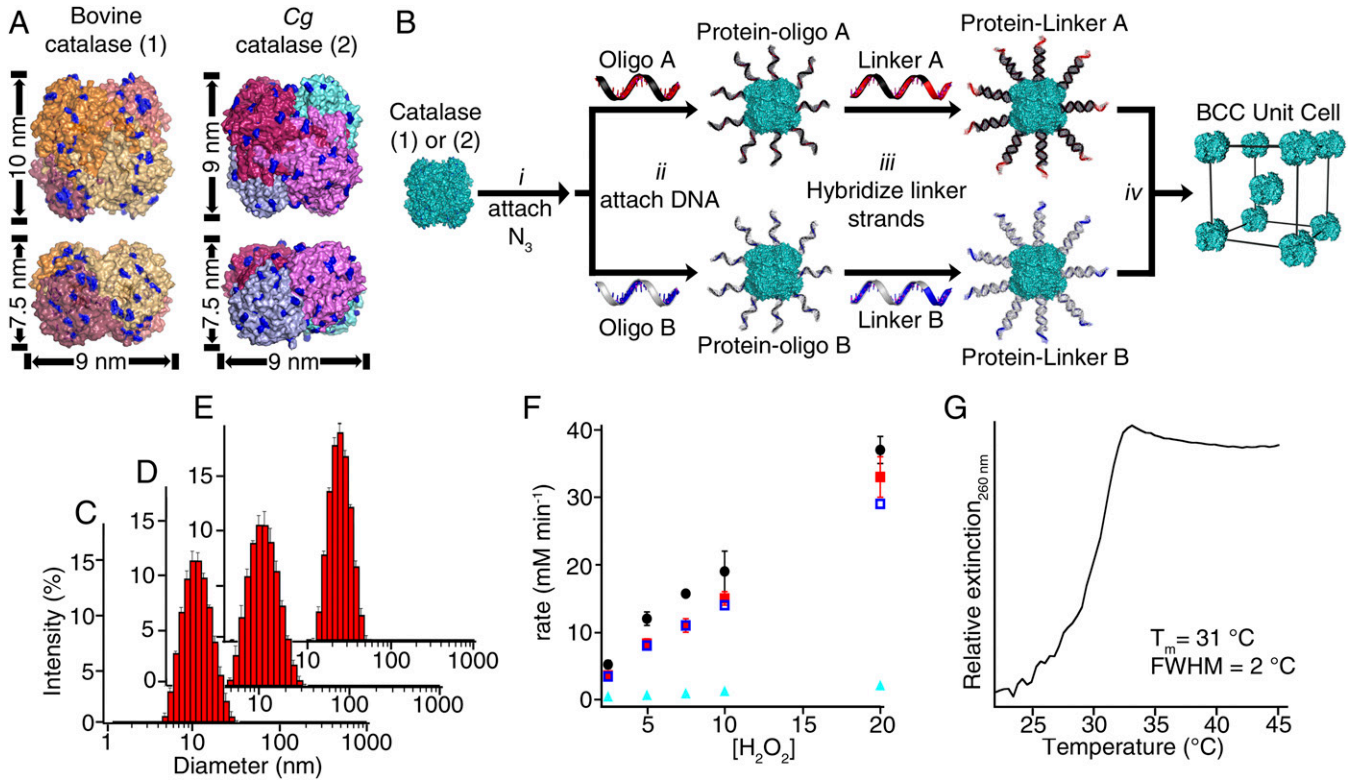

Fig. 1. Synthesis and characterization of protein–DNA conjugates. (*A*) Cartoon depictions of bovine and *Cg* catalases showing their molecular topologies and the locations of surface-accessible amines (blue sticks). (*B*) Scheme for the synthesis and assembly of DNA-functionalized catalases. Surface-accessible amines were modified with azides containing NHS and N_3 moieties at opposing termini (*i*), after which the covalently attached azides were conjugated to two distinct 5′-DBCO–modified DNA strands via a copper-free "click chemistry" reaction (*ii*). Hybridization of linker strands to the DNA-functionalized proteins (*iii*) followed by mixing of proteins with complementary linkers (*iv*) results in the assembly of the proteins into BCC or CsCl-type unit cells. (*C*–*E*) Comparison of the hydrodynamic diameters of native (*C*), N_3-functionalized (*D*), and DNA-functionalized (*E*) *Cg* catalases, as determined by DLS. (*F*) Comparison of the enzyme-catalyzed rates of the disproportionation of H_2O_2 as a function of substrate concentration by native (black circles), DNA-functionalized [red (strand 1) and blue (strand 2) squares], and crystalline (cyan triangles) *Cg* catalase. (*G*) Thermal melting transition of DNA-templated aggregates composed of *Cg* catalase.

mild conditions, thoroughly characterized the DNA-functionalized proteins to ensure that they maintained their native structures and functions, and subsequently observed their DNA-mediated assembly into single-crystalline superlattices.

Results and Discussion

Two variants of the tetrameric heme-containing enzyme, catalase [bovine catalase and *Corynebacterium glutamicum* ("*Cg*") catalase], were used as a model system for studying the DNA-mediated assembly of proteins (Fig. 1*A*). Each catalase variant shares a similar molecular topology but features a distinct pattern of chemically reactive surface-accessible amine functional groups. By adding a large excess (~3,000-fold relative to the protein concentration) of tetraethylene glycol linkers containing an *N*-hydroxysuccinimide (NHS) ester and an azide moiety at opposing termini (Fig. 1*B*, *i*, and Fig. S2, *Inset*), these surface-accessible amines were converted to azides in high yields (75% and 83% of all solvent-accessible primary amines per tetrameric protein complex for *Cg* and bovine catalases, respectively), as determined by mass spectrometry (Fig. S3). The functionalization of the proteins with azides was highly reproducible (15.3 ± 0.3 and 12.2 ± 0.6 labels for bovine and *Cg* catalases, respectively) over five independent reactions using three different batches of protein. The azide-modified proteins were then separately functionalized with two different oligonucleotides (Table S1) via a strain-promoted cycloaddition reaction (Cu-free "click chemistry") between the surface-bound azides and dibenzocyclooctyne (DBCO; Fig. S2, *Inset*) moieties at the 5′-termini of synthetic oligonucleotides (Fig. 1*B*, *ii*). This strategy yielded DNA functionalization densities of 30–50 pmol/cm^2, as determined by changes in the UV absorbance spectrum of each protein–DNA conjugate (Fig. S3). These values are comparable to those achieved with similarly sized inorganic nanomaterials previously used in DNA-mediated crystallization schemes (12, 29). Further characterization of each protein conjugate by dynamic light scattering (DLS) revealed increases in their hydrodynamic diameters after DNA functionalization from 11.7 or 12 nm to 24.3 and 25 nm for bovine and *Cg* catalases, respectively, which is consistent with the formation of a shell of oligonucleotides oriented radially from the protein cores (Fig. 1 *C*–*E* and Fig. S2).

The azide- and DNA-modified proteins were extensively characterized to ensure that they remained folded and functional. The structure of each protein was probed by UV-visible and circular dichroism (CD) spectroscopies, which provide structural information pertaining to the environment surrounding the heme active site and the global secondary structure of the protein, respectively (Figs. S4 and S5). Both techniques suggest that the native protein structure remains largely intact upon functionalization with azides or DNA. Retention of the catalytic functionality of the DNA-functionalized proteins was determined spectrophotometrically by monitoring decreases in the UV absorbance (at 240 nm) of hydrogen peroxide (H_2O_2, ε_{240} = 43 $M^{-1}\cdot cm^{-1}$) upon its catalase-catalyzed disproportionation into H_2O and O_2 (Fig. 1*F* and Fig. S6) (30). The initial rate of this reaction is first order with respect to the H_2O_2 concentration when millimolar concentrations of substrate and relatively low (nanomolar) concentrations of

enzyme are used. The standard velocity constants were similar for DNA-functionalized enzymes and their native counterparts, and agreed well with previously published reports (30), strongly suggesting that the dense shell of DNA appended to the surface of each catalase variant does not significantly affect substrate access to the active site or cause detrimental changes in its structure. In contrast, when the DNA-functionalized proteins were heated above their unfolding temperatures before the assay, no H_2O_2 decomposition was observed (Fig. S6). This finding demonstrates that the rate enhancements observed in the presence of the DNA-functionalized proteins originate from intact active sites, rather than from peroxidase activity resulting from free heme or heme embedded in a matrix of unfolded proteins and DNA.

We next determined whether the protein–DNA conjugates adopted the DNA-dependent properties characteristic of SNA–inorganic NP conjugates. These conjugates form multivalent interactions with particles bearing complementary oligonucleotides, and these interactions are characterized by a highly cooperative transition between the assembled and disassembled states upon gradual increases in temperature. Each protein–DNA conjugate was independently hybridized to a complementary oligonucleotide bearing a single-stranded sticky end sequence (5′-AAGGAA-3′ or 5′-TTCCTT-3′; Fig. 1*B*, *iii*, and Table S1). When proteins bearing linkers with complementary sticky ends were combined, or when either protein was combined with a SNA–gold nanoparticle (AuNP) (10-nm diameter) conjugate with complementary sticky ends, a rapid increase in the turbidity of the solution and a gradual accumulation of aggregates were observed. Significantly, this aggregation event did not occur when particles with noncomplementary sticky ends were combined, ruling out the possibility of nonspecific interactions between proteins, proteins and the AuNP surface, or proteins and DNA. Solutions containing these DNA-templated aggregates were slowly heated, resulting in a sharp increase in their extinction at 260 nm (Fig. 1*G* and Fig. S7). For aggregates containing only DNA-functionalized proteins, this transition results from dehybridization of double-stranded DNA into hyperchromatic single-stranded DNA upon dissociation of the aggregates, whereas for aggregates containing a mixture of DNA-functionalized proteins and SNA–AuNP conjugates, the increase in the extinction is largely due to changes in the optical properties of the AuNPs. The melting temperatures and full-width at half-maximum (FWHM) values for these transitions were similar to those observed for SNA–NP conjugates with inorganic cores (12, 29).

We next determined whether the design rules developed for SNA–inorganic NP conjugates (8, 28) also apply to the assembly of DNA-functionalized proteins. We have previously shown that when spherical SNA–AuNP conjugates with identical sizes are separately functionalized with linkers bearing non–self-complementary sticky ends, the thermodynamically favorable lattice is body-centered cubic. We define these lattices as body-centered cubic (BCC) type rather than cesium chloride (CsCl) because the core NPs are identical, despite the fact that they are functionalized with distinct DNA sequences. To test whether DNA-functionalized proteins form similar lattices, aggregates containing an equimolar ratio of two proteins, or a binary system consisting of a protein and a SNA–AuNP conjugate, were heated to a temperature above their melting point, but below the temperature at which protein unfolding begins, and slowly cooled to 20 °C at a rate of 0.01 °C/min to promote the formation of the thermodynamically stable product. We have recently shown that, compared with an alternative procedure where aggregates are annealed at a temperature slightly below their melting temperature, slowly cooling NP-containing solutions from a dissociated state favors the formation of single crystals over polycrystalline aggregates (11). The rate of 0.01 °C/min was determined empirically, after observing that faster cooling rates yielded ill-defined single crystals or polycrystalline aggregates (11). Using this procedure, *Cg* catalase assembled into superlattices with BCC symmetries and an interparticle spacing of 25.4 nm, as determined from the radially averaged 1D small angle X-ray scattering (SAXS) pattern (Fig. 2*A*). This interparticle spacing is consistent with the measured hydrodynamic diameter of DNA-modified *Cg* catalase (Fig. 1*E* and Fig. S2). An additional diffraction peak at 0.022 $Å^{-1}$ and a shoulder at 0.03 $Å^{-1}$ were also observed, suggesting the presence of a separate lattice isostructural with CsCl. Crystals formed from the three additional protein–protein combinations also produced scattering patterns characteristic of CsCl-type lattices, although the presence of a BCC lattice with similar interparticle spacings cannot be ruled out (Fig. 2 *B*–*D* and Table S2). The formation of lattices with CsCl-type symmetries, rather than BCC symmetry, from nearly identical protein variants suggests that, although the proteins located at each unique lattice position are forming connections with eight nearest neighbors, as expected, they are also adopting distinct orientations. This observation suggests that the unique shape anisotropy and nonuniform surface chemistry of the protein

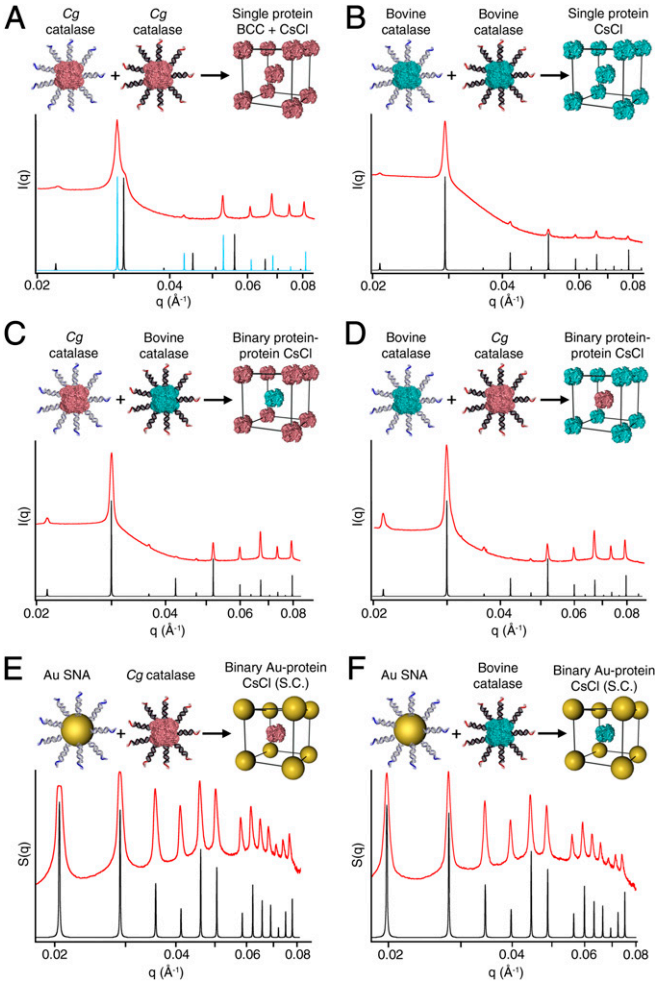

Fig. 2. SAXS data for protein–protein (*A*–*D*) and protein–AuNP (*E* and *F*) superlattices. Each panel shows a comparison between the experimentally observed 1D SAXS patterns (red) and theoretical predictions (black or cyan traces) for protein-containing superlattices. A schematic representation of the components and unit cell of each superlattice type is shown at the *Top* of each panel, where *Cg* catalase, bovine catalase, and AuNPs are depicted as a red cartoon, cyan cartoon, or gold sphere, respectively. The superlattices are isostructural with (*A*) a mixture of BCC (blue theoretical trace) and CsCl (black theoretical trace), (*B*–*D*) CsCl, and (*E* and *F*) simple cubic.

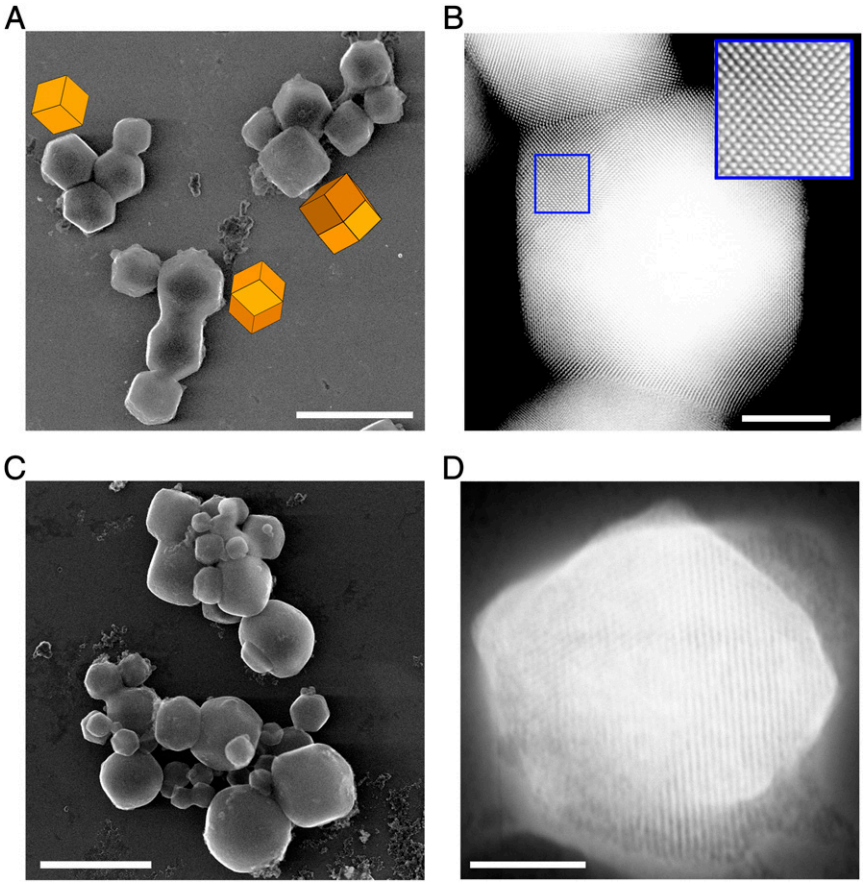

Fig. 3. Characterization of single crystalline superlattices by TEM. Low (*A*)- and high (*B*)-magnification TEM micrographs of *Cg* catalase–AuNP hybrid superlattices showing the uniform formation of the expected rhombic dodecahedron crystal habit. Cartoon depictions of the various orientations of a rhombic dodecahedron are shown side-by-side with experimentally observed superlattices with matching orientations. The *Inset* in *B* depicts the high degree of short-range order between AuNPs within a single crystal. (*C* and *D*) Low- and high-magnification TEM images of superlattices composed of *Cg* catalase. (*D*) A high-magnification TEM image of a single *Cg* catalase crystal with clearly visible lattice planes demonstrating its single crystalline nature. (Scale bars: 5 μm for *A* and *C*, 500 nm for *B*, and 200 nm for *D*).

building blocks affects DNA-mediated superlattice assembly in a manner that has not been observed using traditional SNA–NP conjugates and could be leveraged in future design efforts to form lattices with novel symmetries.

Because the scattering cross-sections of proteins relative to AuNPs are negligible, protein–AuNP binary lattices are expected to produce scattering patterns that are dependent solely on the arrangement of AuNPs within the lattice. Indeed, when DNA-functionalized proteins were combined in a 1:1 ratio with SNA–AuNP conjugates bearing linkers with complementary sticky ends, the resulting CsCl-type lattices produced simple cubic scattering patterns (Fig. 2 *E* and *F*). In these lattices, the protein acts as a 3D spacer that effectively deletes lattice positions that would otherwise be occupied by AuNPs. The ability to combine two types of nanomaterials with such disparate physical and chemical properties, without significantly altering the compact 3D structure of the soft protein-based building block, highlights the broad generalizability of DNA-mediated assembly and could be useful in assembling multifunctional materials.

The microscale morphologies of the protein crystals were investigated by scanning transmission electron microscopy of silica embedded (for binary protein–Au systems) or negatively stained (for lattices composed only of DNA-functionalized proteins) specimens (Fig. 3 and Fig. S8). Micrographs of both samples demonstrate the uniform formation of single crystals 1–7 μm in each dimension. Binary protein–AuNP crystals displayed clear facets and hexagonal and square domains, similar to those previously observed for SNA–AuNP conjugates that assemble into rhombic dodecahedra (11). This occurs despite the fact that for Au–protein binary crystals, the inclusion of a protein spacer results in a simple cubic arrangement of AuNPs. High-magnification images of a single crystal with a binary protein–AuNP composition (Fig. 3*B*) revealed a remarkable degree of order, with stacks of individual NPs clearly discernible (Fig. 3*B*, *Inset*). Similarly, lattice planes could be visualized in negatively stained specimens prepared from *Cg* catalase crystals (Fig. 3*D*).

The crystals composed of *Cg* catalase were used in H_2O_2 decomposition assays, as described above, to determine whether the enzymes remained active after the crystallization process. As with native or DNA-functionalized enzymes free in solution, the rate of H_2O_2 decomposition by the crystals showed a linear dependence on the substrate concentration (Fig. 1*F* and Fig. S6*I*), although the apparent rate constants were reduced by a factor of ∼20. Similar decreases in catalytic efficiency have previously been observed in studies of crystalline enzyme preparations, especially for highly efficient enzymes where diffusion into the crystal is a limiting factor (31). Significantly, the enzymes could be easily recycled after catalysis by centrifugation and retained full catalytic activity throughout at least five rounds of catalysis (Fig. S6*J*). Analysis of the insoluble material by SAXS after the

final round of catalysis confirmed that the crystal lattice remained intact (Fig. S6*K*).

Conclusions

Despite notable recent achievements (32, 33), the de novo design of protein–protein interactions, especially to form supramolecular structures beyond dimeric complexes, remains difficult due to a lack of universal interaction motifs (34). In contrast, oligonucleotide base-pairing interactions are well understood, form with high fidelity, and have been widely used as a means for assembling diverse supramolecular shapes that can act as scaffolds for organizing the assembly of external molecules, including proteins or protein-based virus capsids (35–40). By replacing the formation of protein–protein interactions with oligonucleotide hybridization, we have shown that crystalline superlattices can be assembled from a single protein, multiple proteins, or a combination of proteins and AuNPs. This strategy should provide a means for programming the assembly of complex biomaterials (e.g., enzyme cascades or hybrid inorganic–organic lattices) from functional proteins regardless of their amino acid compositions or molecular topologies. Future modifications to this strategy could also take advantage of the anisotropic shapes and nonuniform surface chemistries of proteins to enable the formation of lattices not previously explored.

Materials and Methods

All oligonucleotides were synthesized on solid supports on a Mermade 48 (MM48) oligonucleotide synthesizer using reagents obtained from Glen Research and purified by RP-HPLC. Citrate-capped AuNPs with 10-nm nominal diameters were obtained from Ted Pella and functionalized with DNA as previously described (4, 8). Briefly, ∼5 nmol of the appropriate 5′-thiolated oligonucleotide were added per milliliter (mL) of AuNPs, after which SDS was added to a final concentration of 0.01%, and the resulting solution was incubated for 4 h at room temperature. Aliquots of 5 M NaCl were added to the solution in 0.1-M steps over the course of 3 h to reach a final concentration of 0.5 M NaCl. This solution was then allowed to incubate overnight at room temperature to maximize DNA loading on the surface of the AuNPs. The DNA-functionalized particles were purified by three rounds of centrifugation at 21,130 × *g*, followed by resuspension of the resulting pellet in 1 mL of PBS. Particle concentrations were determined based on UV-visible absorbance spectra (Varian Cary 5000) using a molar extinction coefficient (ε_{520}) of 9.55 × 10^7 $M^{-1}\cdot cm^{-1}$ (provided by Ted Pella; www.tedpella.com/gold_html/gold-tec.htm).

Bovine and *Cg* catalases (Sigma) were exchanged into PBS by ultrafiltration (Amicon Ultra; 100 kDa) and their purity confirmed by SDS/PAGE. Both proteins ran as a single molecular species with the expected molecular weights (∼60 kDa per monomer) and were therefore used as received. Before chemical functionalization, each protein was concentrated and exchanged into a buffer containing 100 mM sodium bicarbonate (pH 9, 0.5 M NaCl) by ultrafiltration. Protein concentrations were determined by UV-visible absorbance spectroscopy using a molar extinction coefficient (ε_{405}) of 324,000 $M^{-1}\cdot cm^{-1}$ (41).

To a 100-μL solution containing 50 μM protein in 100 mM sodium bicarbonate buffer (pH 9, 0.5 M NaCl) was added approximately 6 mg of the linker NHS-PEG_4-N_3 (Thermo Scientific; Fig. S2, *Inset*). The reaction between surface amines and NHS-PEG_4-N_3 was allowed to proceed at 25 °C for 2 h while shaking at 1,000 rpm on a Benchmark Multi-therm shaker. The azide-functionalized proteins were purified by size exclusion chromatography using NAP10 columns (GE Healthcare) equilibrated with PBS (pH 7.4). The number of attached linkers was determined by MALDI-MS on a Bruker Autoflex III mass spectrometer (Fig. S3) based on an added mass of 274 Da per linker.

Each azide-modified protein was separately functionalized with two distinct oligonucleotides containing a 5′-terminal DBCO moiety. Typical reactions contained 3 nmol of protein and 1 μmol of the indicated oligonucleotide in PBS (0.5 M NaCl). The reactions were incubated for 3 d at 25 °C while shaking at 1,000 rpm on a Benchmark Multi-therm shaker, after which unreacted DNA was removed from the reaction solutions by 10 rounds of ultrafiltration (Millipore Amicon Ultra-15 Centrifugal Filter Units). The oligonucleotide/protein ratio of each DNA-functionalized protein was determined by UV-visible absorbance spectroscopy (Fig. S3).

DLS experiments were performed on a Malvern Zetasizer Nano. Each sample contained 1 μM of the native, azide-functionalized or DNA-functionalized catalase. The reported spectra and hydrodynamic diameters (Fig. 1 *C–E* and Fig. S2) are based on intensity distributions and are the average of three measurements.

UV-visible absorbance and CD spectroscopies were used to probe the structures of the native, N_3-, and DNA-functionalized catalase variants (Figs. S4 and S5). UV-visible absorbance spectra were recorded in a 1-cm-path length cuvette containing a solution of ∼1 μM protein in PBS (0.5 M NaCl). CD spectra were recorded on a Jasco J-818 spectrophotometer in a 1-mm-path length cuvette. All protein-containing samples were prepared at a concentration of 300 nM in PBS (0.5 M NaCl). The raw ellipticity values (millidegrees) were converted to $\Delta\varepsilon$ ($mM^{-1}\cdot cm^{-1}$) and the resulting spectra smoothed using a Savitzky–Golay algorithm in Igor Pro (Wavemetrics). Spectra of the azide-functionalized proteins were compared directly to their native counterparts (Fig. S4).

CD spectra of the unconjugated 5′-DBCO–containing oligonucleotides were collected from samples prepared at a concentration of ∼15 μM. The $\Delta\varepsilon$ value of each DNA strand was then multiplied by the DNA/protein ratio calculated for each protein variant (Table S1). The theoretical spectrum of each DNA-functionalized protein was calculated by summation of the spectrum of the native protein and the spectrum of DNA multiplied by the expected DNA/protein ratio (Fig. S5).

The disproportionation of H_2O_2 to H_2O and O_2 was followed spectrophotometrically, essentially as previously described (30). Briefly, a 10-μL aliquot of native or DNA-functionalized catalase was added from a stock solution (100 nM) to a stirred cuvette containing the indicated concentration of H_2O_2 in 1000 μL of PBS (0.5 M NaCl). After the addition of catalase, the absorbance at 240 nm was monitored continuously for 1 min. Reaction rates were then calculated from the slopes of the initial linear portions of these traces, using a H_2O_2 ε_{240} value of 43 $M^{-1}\cdot cm^{-1}$. Each data point represents the average of three trials (Fig. S6). Standard velocity constants (k_{app}) were calculated for each H_2O_2 concentration, and the average is reported in Fig. S6*H*. To test whether the observed catalytic activity was due to the presence of intact folded catalase, and not free porphyrin or porpyrin embedded in a matrix of unfolded protein and DNA, enzyme assays were also performed using DNA-functionalized proteins that were unfolded by incubation at 60 °C for 10 min (Fig. S6).

Protein crystals (assembled as described below) were isolated by four rounds of centrifugation at 2,348 × *g*. The total concentration of protein contained in the purified crystals was determined by recording their UV-visible absorbance spectrum at 40 °C. The crystals were then diluted to a final protein concentration of 100 nM and their catalytic activity was tested (Fig. 1*F* and Fig. S6). To test the recyclability of the enzyme crystals, they were incubated with 15 mM H_2O_2 for 10 min and centrifuged to collect the remaining insoluble material. After this treatment, both the supernatant and insoluble materials were tested for catalytic activity (Fig. S6*J*). This process was repeated five times, after which a SAXS spectrum was collected to ensure that the crystal lattice remained intact (Fig. S6*K*).

DNA-functionalized proteins and AuNP–SNA conjugates were hybridized to complementary linker strands by adding 100 eq of the appropriate linker to a solution containing 300 nM of the indicated protein in PBS (0.5 M NaCl). Protein-containing aggregates were assembled by mixing a single DNA-functionalized protein separately hybridized to two different linkers, two different DNA-functionalized proteins, each of which was hybridized with a linker complementary to the other, or a DNA-functionalized protein and a SNA–AuNP conjugate separately hybridized to complementary linkers. The resulting aggregates were added to 1,000 μL of PBS (0.5 M NaCl) to a final particle concentration of 15 nM and their melting temperatures determined by UV-visible absorbance spectroscopy (Fig. 1*G* and Fig. S7). The first derivative of each melting curve was calculated to determine the T_m and FWHM of each sample.

Crystals were assembled by heating DNA-templated aggregates composed of either linker-hybridized DNA-functionalized proteins or a linker-hybridized protein and a SNA–AuNP conjugate above their melting temperatures (43 °C) and slowly cooling them to room temperature at a rate of 0.01 °C/min. This procedure was recently shown to favor the formation of single crystalline over polycrystalline superlattices (11).

SAXS experiments were carried out at the DuPont–Northwestern–Dow Collaborative Access Team (DND-CAT) beam line of Argonne National Laboratory's Advanced Photon Source (APS). Experiments were performed with 10 keV (wavelength, 1.24 Å) collimated X-rays calibrated against a silver behenate standard. Samples were transferred to 1.5-mm quartz capillaries (Charles Supper) and their 2D scattering patterns recorded in situ on a CCD area detector. Exposure times used were 0.5 and 5 s for Au–protein hybrid and protein-only lattices, respectively. The 1D scattering data presented in Fig. 2 were obtained by radial averaging of the 2D data to obtain plots of scattering intensity as a function of the scattering vector *q*:

$$q = 4\pi \sin\theta/\lambda,$$

where θ is one-half of the scattering angle and λ is the wavelength of the X-rays used.

All theoretical X-ray diffraction patterns were calculated using the *PowderCell* software package available free of charge from the Federal Institute for Materials Research and Testing (www.ccp14.ac.uk/ccp/web-mirrors/powdcell/a_v/v_1/powder/e_cell.html). Although this software was initially developed for calculating structure factors for lattices based on atomic constituents, it has also been shown to generate theoretical scattering patterns for NP superlattices that match well with experimental data. For binary superlattices assembled from proteins and AuNPs, where the resulting scattering pattern is dominated by the AuNPs and is characteristic of a simple cubic lattice, the atom choice is arbitrary. The same is true for BCC-type lattices composed of a single protein. To generate simulated diffraction patterns for CsCl-type lattices composed of a single protein or two proteins, atoms with similar electron densities were chosen. The positions of the diffraction peaks in the simulated scattering patterns matched well with those experimentally observed.

The nearest neighbor distance d for each lattice type was calculated based on the position of the first scattering peak q_0 using the following equation:

$$d = \left(\frac{1}{10}\right)\left(\frac{C}{q_0}\right),$$

where d is the distance in nanometers between two particles, q_0 is the position of the initial scattering peak in 1/angstrom, and C is a constant that correlates the distance between two NP nearest neighbors and the distance between the [*hkl*] planes associated with the first scattering peak. Values of C, q_o, d, and lattice parameters are summarized in Table S2.

Transmission electron microscopy (TEM) imaging was performed on a Hitachi HD2300 scanning transmission electron microscope operated at 200 keV in SE or *Z*-contrast mode. Binary superlattices composed of SNA–AuNP conjugates and DNA-functionalized proteins were embedded in amorphous silica as previously described (11, 42). This procedure is necessary to prevent the DNA-mediated lattices from collapsing during sample preparation and imaging under vacuum. A 5-μL aliquot of these silica-embedded superlattices was drop cast onto a carbon-coated copper mesh grid, and excess liquid was removed by blotting with Whatman filter paper. Superlattices composed solely of DNA-functionalized proteins were stained with a 2% (wt/vol) solution of uranyl acetate to obtain sufficient contrast for imaging.

ACKNOWLEDGMENTS. We thank Byeongdu Lee for assistance with interpretation of the SAXS data. C.A.M. acknowledges support from the Office of the Assistant Secretary of Defense for Research and Engineering, Department of Defense/National Security Science and Engineering Faculty Fellowship Program under Award N00014-15-1-0043, and the Air Force Office of Scientific Research under Award FA9550-11-1-0275. SAXS experiments were carried out at the Dupont–Northwestern–Dow Collaborative Access Team beam line at the APS, Argonne National Laboratory. Use of the APS was supported by the Department of Energy (DE-AC02-06CH11357). The TEM work was performed in the Electron Probe Instrumentation Center facility of the NUANCE Center at Northwestern University.

1. Mirkin CA, Letsinger RL, Mucic RC, Storhoff JJ (1996) A DNA-based method for rationally assembling nanoparticles into macroscopic materials. *Nature* 382(6592):607–609.
2. Seeman NC (2007) An overview of structural DNA nanotechnology. *Mol Biotechnol* 37(3):246–257.
3. Jones MR, Seeman NC, Mirkin CA (2015) Programmable materials and the nature of the DNA bond. *Science*, 10.1126/science.1260901.
4. Park SY, et al. (2008) DNA-programmable nanoparticle crystallization. *Nature* 451(7178):553–556.
5. Nykypanchuk D, Maye MM, van der Lelie D, Gang O (2008) DNA-guided crystallization of colloidal nanoparticles. *Nature* 451(7178):549–552.
6. Hill HD, et al. (2008) Controlling the lattice parameters of gold nanoparticle FCC crystals with duplex DNA linkers. *Nano Lett* 8(8):2341–2344.
7. Macfarlane RJ, et al. (2010) Establishing the design rules for DNA-mediated programmable colloidal crystallization. *Angew Chem Int Ed Engl* 49(27):4589–4592.
8. Macfarlane RJ, et al. (2011) Nanoparticle superlattice engineering with DNA. *Science* 334(6053):204–208.
9. Xiong H, van der Lelie D, Gang O (2009) Phase behavior of nanoparticles assembled by DNA linkers. *Phys Rev Lett* 102(1):015504.
10. Auyeung E, et al. (2012) Synthetically programmable nanoparticle superlattices using a hollow three-dimensional spacer approach. *Nat Nanotechnol* 7(1):24–28.
11. Auyeung E, et al. (2014) DNA-mediated nanoparticle crystallization into Wulff polyhedra. *Nature* 505(7481):73–77.
12. Zhang C, et al. (2013) A general approach to DNA-programmable atom equivalents. *Nat Mater* 12(8):741–746.
13. Zhang Y, Lu F, Yager KG, van der Lelie D, Gang O (2013) A general strategy for the DNA-mediated self-assembly of functional nanoparticles into heterogeneous systems. *Nat Nanotechnol* 8(11):865–872.
14. Winfree E, Liu F, Wenzler LA, Seeman NC (1998) Design and self-assembly of two-dimensional DNA crystals. *Nature* 394(6693):539–544.
15. Zheng J, et al. (2009) From molecular to macroscopic via the rational design of a self-assembled 3D DNA crystal. *Nature* 461(7260):74–77.
16. Mann S (2008) Life as a nanoscale phenomenon. *Angew Chem Int Ed Engl* 47(29):5306–5320.
17. Liljeström V, Mikkilä J, Kostiainen MA (2014) Self-assembly and modular functionalization of three-dimensional crystals from oppositely charged proteins. *Nat Commun* 5:4445.
18. Kostiainen MA, et al. (2013) Electrostatic assembly of binary nanoparticle superlattices using protein cages. *Nat Nanotechnol* 8(1):52–56.
19. Brodin JD, et al. (2012) Metal-directed, chemically tunable assembly of one-, two- and three-dimensional crystalline protein arrays. *Nat Chem* 4(5):375–382.
20. Dotan N, Arad D, Frolow F, Freeman A (1999) Self-assembly of a tetrahedral lectin into predesigned diamondlike protein crystals. *Angew Chem Int Ed Engl* 38(16):2363–2366.
21. Ringler P, Schulz GE (2003) Self-assembly of proteins into designed networks. *Science* 302(5642):106–109.
22. Sakai F, et al. (2014) Protein crystalline frameworks with controllable interpenetration directed by dual supramolecular interactions. *Nat Commun* 5:4634.
23. Oohora K, Onoda A, Hayashi T (2012) Supramolecular assembling systems formed by heme-heme pocket interactions in hemoproteins. *Chem Commun (Camb)* 48(96):11714–11726.
24. Padilla JE, Colovos C, Yeates TO (2001) Nanohedra: Using symmetry to design self assembling protein cages, layers, crystals, and filaments. *Proc Natl Acad Sci USA* 98(5):2217–2221.
25. Sinclair JC, Davies KM, Vénien-Bryan C, Noble MEM (2011) Generation of protein lattices by fusing proteins with matching rotational symmetry. *Nat Nanotechnol* 6(9):558–562.
26. Strable E, Johnson JE, Finn MG (2004) Natural nanochemical building blocks: Icosahedral virus particles organized by attached oligonucleotides. *Nano Lett* 4(8):1385–1389.
27. Cigler P, Lytton-Jean AKR, Anderson DG, Finn MG, Park SY (2010) DNA-controlled assembly of a NaTl lattice structure from gold nanoparticles and protein nanoparticles. *Nat Mater* 9(11):918–922.
28. Macfarlane RJ, O'Brien MN, Petrosko SH, Mirkin CA (2013) Nucleic acid-modified nanostructures as programmable atom equivalents: Forging a new "table of elements." *Angew Chem Int Ed Engl* 52(22):5688–5698.
29. Hurst SJ, Lytton-Jean AKR, Mirkin CA (2006) Maximizing DNA loading on a range of gold nanoparticle sizes. *Anal Chem* 78(24):8313–8318.
30. Beers RF, Jr, Sizer IW (1952) A spectrophotometric method for measuring the breakdown of hydrogen peroxide by catalase. *J Biol Chem* 195(1):133–140.
31. Mozzarelli A, Rossi GL (1996) Protein function in the crystal. *Annu Rev Biophys Biomol Struct* 25:343–365.
32. King NP, et al. (2012) Computational design of self-assembling protein nanomaterials with atomic level accuracy. *Science* 336(6085):1171–1174.
33. King NP, et al. (2014) Accurate design of co-assembling multi-component protein nanomaterials. *Nature* 510(7503):103–108.
34. Stranges PB, Kuhlman B (2013) A comparison of successful and failed protein interface designs highlights the challenges of designing buried hydrogen bonds. *Protein Sci* 22(1):74–82.
35. Wilner OI, et al. (2009) Enzyme cascades activated on topologically programmed DNA scaffolds. *Nat Nanotechnol* 4(4):249–254.
36. Zhang C, et al. (2012) DNA-directed three-dimensional protein organization. *Angew Chem Int Ed Engl* 51(14):3382–3385.
37. Rusling DA, et al. (2014) Functionalizing designer DNA crystals with a triple-helical veneer. *Angew Chem Int Ed Engl* 53(15):3979–3982.
38. Yan H, Park SH, Finkelstein G, Reif JH, LaBean TH (2003) DNA-templated self-assembly of protein arrays and highly conductive nanowires. *Science* 301(5641):1882–1884.
39. Wang D, et al. (2014) Hierarchical assembly of plasmonic nanostructures using virus capsid scaffolds on DNA origami templates. *ACS Nano* 8(8):7896–7904.
40. Coyle MP, Xu Q, Chiang S, Francis MB, Groves JT (2013) DNA-mediated assembly of protein heterodimers on membrane surfaces. *J Am Chem Soc* 135(13):5012–5016.
41. Samejima T, Yang JT (1963) Reconstitution of acid-denatured catalase. *J Biol Chem* 238(10):3256–3261.
42. Auyeung E, Macfarlane RJ, Choi CHJ, Cutler JI, Mirkin CA (2012) Transitioning DNA-engineered nanoparticle superlattices from solution to the solid state. *Adv Mater* 24(38):5181–5186.